**Astronomy & Astrophysics**

# *Planck* intermediate results

## I. Further validation of new *Planck* clusters with *XMM-Newton*

Planck Collaboration: N. Aghanim[54], M. Arnaud[69,*], M. Ashdown[66,5], F. Atrio-Barandela[17], J. Aumont[54],
C. Baccigalupi[79], A. Balbi[34], A. J. Banday[87,8], R. B. Barreiro[62], J. G. Bartlett[1,64], E. Battaner[89], K. Benabed[55,85],
J.-P. Bernard[8], M. Bersanelli[31,48], H. Böhringer[75], A. Bonaldi[65], J. R. Bond[7], J. Borrill[13,83], F. R. Bouchet[55,85],
H. Bourdin[34], M. L. Brown[65], C. Burigana[47,33], R. C. Butler[47], P. Cabella[35], J.-F. Cardoso[70,1,55], P. Carvalho[5],
A. Catalano[71,68], L. Cayón[24], A. Challinor[52], R.-R. Chary[53], L.-Y. Chiang[58], G. Chon[75], P. R. Christensen[76,36],
D. L. Clements[52], S. Colafrancesco[44], S. Colombi[55], A. Coulais[68], B. P. Crill[64,77], F. Cuttaia[47], A. Da Silva[11],
H. Dahle[60,10], R. J. Davis[65], P. de Bernardis[30], G. de Gasperis[34], G. de Zotti[43,79], J. Delabrouille[1], J. Démoclès[69],
F.-X. Désert[51], J. M. Diego[62], K. Dolag[88,74], H. Dole[54], S. Donzelli[48], O. Doré[64,9], M. Douspis[54], X. Dupac[40],
T. A. Enßlin[74], H. K. Eriksen[60], F. Finelli[47], I. Flores-Cacho[8,87], O. Forni[87,8], P. Fosalba[56], M. Frailis[45],
S. Fromenteau[1,54], S. Galeotta[45], K. Ganga[1], R. T. Génova-Santos[61], M. Giard[87,8], J. González-Nuevo[62,79],
R. González-Riestra[39], K. M. Górski[64,91], A. Gregorio[32], A. Gruppuso[47], F. K. Hansen[60], D. Harrison[59,66],
A. Hempel[61,37], C. Hernández-Monteagudo[12,74], D. Herranz[62], S. R. Hildebrandt[9], A. Hornstrup[16],
K. M. Huffenberger[90], G. Hurier[71], T. Jagemann[40], J. Jasche[4], M. Juvela[23], E. Keihänen[23], R. Keskitalo[64,9],
T. S. Kisner[73], R. Kneissl[38,6], J. Knoche[74], L. Knox[26], H. Kurki-Suonio[23,42], G. Lagache[54], A. Lähteenmäki[2,42],
J.-M. Lamarre[68], A. Lasenby[5,66], C. R. Lawrence[64], S. Leach[79], R. Leonardi[40], A. Liddle[22], P. B. Lilje[60,10],
M. López-Caniego[62], G. Luzzi[67], J. F. Macías-Pérez[71], D. Maino[31,48], N. Mandolesi[47], R. Mann[80], F. Marleau[19],
D. J. Marshall[87,8], E. Martínez-González[62], S. Masi[30], M. Massardi[46], S. Matarrese[29], F. Matthai[74], P. Mazzotta[34],
P. R. Meinhold[27], A. Melchiorri[30,49], J.-B. Melin[15], L. Mendes[40], A. Mennella[31,48], M.-A. Miville-Deschênes[54,7],
A. Moneti[55], L. Montier[87,8], G. Morgante[47], D. Mortlock[52], D. Munshi[81], P. Naselsky[76,36], P. Natoli[33,3,47],
H. U. Nørgaard-Nielsen[16], F. Noviello[65], S. Osborne[84], F. Pasian[45], G. Patanchon[1], O. Perdereau[67], F. Perrotta[79],
F. Piacentini[30], E. Pierpaoli[21], S. Plaszczynski[67], P. Platania[63], E. Pointecouteau[87,8], G. Polenta[3,44], N. Ponthieu[54,51],
L. Popa[57], T. Poutanen[42,23,2], G. W. Pratt[69], J.-L. Puget[54], J. P. Rachen[74], R. Rebolo[61,14,37], M. Reinecke[74],
M. Remazeilles[54,1], C. Renault[71], S. Ricciardi[47], T. Riller[74], I. Ristorcelli[87,8], G. Rocha[64,9], C. Rosset[1],
M. Rossetti[31,48], J. A. Rubiño-Martín[61,37], B. Rusholme[53], M. Sandri[47], G. Savini[78], B. M. Schaefer[86], D. Scott[20],
G. F. Smoot[25,73,1], J.-L. Starck[69], F. Stivoli[50], R. Sunyaev[74,82], D. Sutton[59,66], J.-F. Sygnet[55], J. A. Tauber[41],
L. Terenzi[47], L. Toffolatti[18,62], M. Tomasi[48], M. Tristram[67], L. Valenziano[47], B. Van Tent[72], P. Vielva[62], F. Villa[47],
N. Vittorio[34], B. D. Wandelt[55,85,28], J. Weller[88], S. D. M. White[74], D. Yvon[15], A. Zacchei[45], and A. Zonca[27]

*(Affiliations can be found after the references)*

### ABSTRACT

We present further results from the ongoing *XMM-Newton* validation follow-up of *Planck* cluster candidates, detailing X-ray observations of eleven candidates detected at a signal-to-noise ratio of $4.5 < S/N < 5.3$ in the same 10-month survey maps used in the construction of the Early SZ sample. The sample was selected in order to test internal SZ quality flags, and the pertinence of these flags is discussed in light of the validation results. Ten of the candidates are found to be *bona fide* clusters lying below the RASS flux limit. Redshift estimates are available for all confirmed systems via X-ray Fe-line spectroscopy. They lie in the redshift range $0.19 < z < 0.94$, demonstrating *Planck*'s capability to detect clusters up to high $z$. The X-ray properties of the new clusters appear to be similar to previous new detections by *Planck* at lower $z$ and higher SZ flux: the majority are X-ray underluminous for their mass, estimated using $Y_X$ as mass proxy, and many have a disturbed morphology. We find tentative indication for Malmquist bias in the $Y_{SZ}$–$Y_X$ relation, with a turnover at $Y_{SZ} \sim 4 \times 10^{-4}$ arcmin². We present additional new optical redshift determinations with ENO and ESO telescopes of candidates previously confirmed with *XMM-Newton*. The X-ray and optical redshifts for a total of 20 clusters are found to be in excellent agreement. We also show that useful lower limits can be put on cluster redshifts using X-ray data only via the use of the $Y_X$ vs. $Y_{SZ}$ and X-ray flux $F_X$ vs. $Y_{SZ}$ relations.

**Key words.** cosmology: observations – galaxies: clusters: general – galaxies: clusters: intracluster medium – cosmic background radiation – X-rays: galaxies: clusters

## 1. Introduction

The deep potential wells in clusters of galaxies make them unique laboratories in which to study astrophysical processes linked to gas physics, galaxy formation, and feedback.

Furthermore, since clusters trace the highest peaks of the matter density field, the properties of the cluster population and their evolution are a sensitive cosmological probe.

The recent advent of increased sensitivity and survey capability has transformed galaxy cluster searches via the Sunyaev-Zeldovich (SZ) effect. Such surveys identify objects using the spectral distortion of the cosmic microwave background (CMB) generated through inverse Compton scattering of CMB photons by the hot electrons in the intra-cluster medium (Sunyaev & Zeldovich 1972). Crucially, the total SZ signal is expected to be closely related to the cluster mass (e.g., da Silva et al. 2004), and its surface brightness insensitive to distance. As a result, SZ surveys can potentially provide unbiased cluster samples over a wide range of redshifts that are as close as possible to being mass-selected. Such samples are essential for understanding the statistical properties of the cluster population and for its exploitation in cosmological studies. Examples of on-going cluster surveys in the SZ include the Atacama Cosmology Telescope (ACT Marriage et al. 2011), *Planck*[1] (Planck Collaboration 2011c) and the South Pole Telescope (SPT Carlstrom et al. 2011).

The *Planck* satellite has been surveying the sky in the microwave band since August 2009 (Planck Collaboration 2011a). Compared to other SZ surveys, *Planck* has only modest (band-dependent) spatial resolution of 5′ to 30′ (Mennella et al. 2011; Planck HFI Core Team 2011) but it possesses unique nine-band coverage from 30 to 857 GHz and, most crucially, it covers an exceptionally large survey volume. Indeed *Planck* is the first all-sky survey capable of blind cluster detections since the ROSAT All-Sky Survey (RASS, in the X-ray domain). Early *Planck* results on galaxy clusters were recently published in Planck Collaboration (2011b,c,g,d,e,f). These results include the publication of the high signal-to-noise ratio ($S/N > 6$) Early SZ (ESZ) cluster sample (Planck Collaboration 2011b).

The raw data product of any cluster survey is a list of potential candidates. Such a list is expected to include a fraction of false detections, e.g., for SZ detections, due to fluctuations in the complex microwave astrophysical sky. In the case of *Planck*, the moderate spatial resolution at SZ frequencies with respect to typical cluster sizes presents a further complication. A *Planck* cluster SZ measurement essentially provides only a position, a total SZ flux, and a coarse size estimate. In addition, the quality of the SZ flux estimates is degraded by the flux-size degeneracy, as discussed in Planck Collaboration (2011b). A follow-up programme is therefore required to scientifically exploit *Planck* candidate data. Such a programme should provide candidate confirmation, which is the final part of the catalogue validation, and a redshift measurement, the prerequisite to any cluster physical parameter estimate.

In this context, X-ray observations are extremely useful, as has been shown by the results from the initial validation follow-up of *Planck* cluster candidates with *XMM-Newton* (Planck Collaboration 2011c). These observations were undertaken in Director's Discretionary Time via an agreement between the *XMM-Newton* and *Planck* Project Scientists. A pilot programme observed ten targets to refine the selection criteria for the ESZ cluster sample. A second programme focused on

the validation of fifteen high-significance SZ sources ($S/N > 5$); eleven of the newly-discovered clusters from this programme are contained in the ESZ sample. These first observations provided a preview of the X-ray properties of the newly-discovered clusters (Planck Collaboration 2011c). In particular it was confirmed that, based on the detection of extended emission, *XMM-Newton* snapshot exposures (10 ks) are sufficient for unambiguous discrimination between clusters and false candidates for redshifts at least up to $z = 1.5$. In addition, it was shown that the spurious association of candidates with faint extended sources lying within the *Planck* position uncertainty (which can be up to 5′) can be identified via a consistency check between the X-ray and SZ flux. This latter constraint stems from the tight correlation between X-ray and SZ properties, since X-rays probe the same medium as the SZE. In this respect, X-ray validation presents a clear advantage over optical validation for *Planck* candidates. While optical observations offer important complementary information on the stellar component of clusters and on mass estimates derived from gravitational lensing of background sources, optical validation is hampered by the relatively large *Planck* source position uncertainty and the large scatter between simple optical observables (such as galaxy numbers) and the mass (or SZ signal), both of which increase the chance of false associations.

A manageable confirmation programme for the compilation of a larger, final, cluster catalogue from the *Planck* survey requires a candidate sample with a high ratio of true clusters to total candidates (i.e., purity). The construction of such a sample relies both on *Planck* internal candidate selection and assessment of the SZ signal quality and also on cross-correlation with ancillary data and catalogues, as described in Planck Collaboration (2011b). In the present paper, in which we report on a further eleven *XMM-Newton* observations of *Planck* cluster candidates detected at $4.5 < S/N < 5.3$, we address in more detail the internal quality assessment of cluster candidates in SZ. *XMM-Newton* validation, allowing unambiguous discrimination between clusters and false candidates, is essential for such a study.

X-ray observations can also constrain the redshift of the source through Fe K line spectroscopy, as demonstrated in Planck Collaboration (2011c). Here we also present new optical redshift determinations for *XMM-Newton* confirmed candidates, which we compare to the X-ray-derived values. We also discuss whether, in the absence of optical follow-up data, a combined X-ray/SZ analysis can improve the $z$ estimate when X-ray data alone are insufficient to unambiguously determine the redshift.

We adopt a $\Lambda$CDM cosmology with $H_0 = 70$ km s$^{-1}$ Mpc$^{-1}$, $\Omega_M = 0.3$, and $\Omega_\Lambda = 0.7$. The factor $E(z) = \sqrt{\Omega_M(1 + z)^3 + \Omega_\Lambda}$ is the ratio of the Hubble constant at redshift $z$ to its present-day value. The quantities $M_{500}$ and $R_{500}$ are the total mass and radius corresponding to a total density contrast $\delta = 500$, as compared to $\rho_c(z)$, the critical density of the Universe at the cluster redshift; $M_{500} = (4\pi/3)\,500\,\rho_c(z)\,R_{500}^3$. The SZ flux is characterised by $Y_{500}$, where $Y_{500}\,D_A^2$ is the spherically integrated Compton parameter within $R_{500}$, and $D_A$ is the angular-diameter distance to the cluster.

## 2. Sample selection

The present candidates were chosen from the catalogue of detections in the all-sky maps from the first ten months of the *Planck* survey. This same catalogue was used for the construction of the ESZ sample, for which the reference method for blind cluster searches was the matched multi-frequency filter

---

[1] *Planck* (http://www.esa.int/Planck) is a project of the European Space Agency (ESA) with instruments provided by two scientific consortia funded by ESA member states (in particular the lead countries: France and Italy) with contributions from NASA (USA), and telescope reflectors provided in a collaboration between ESA and a scientific consortium led and funded by Denmark.
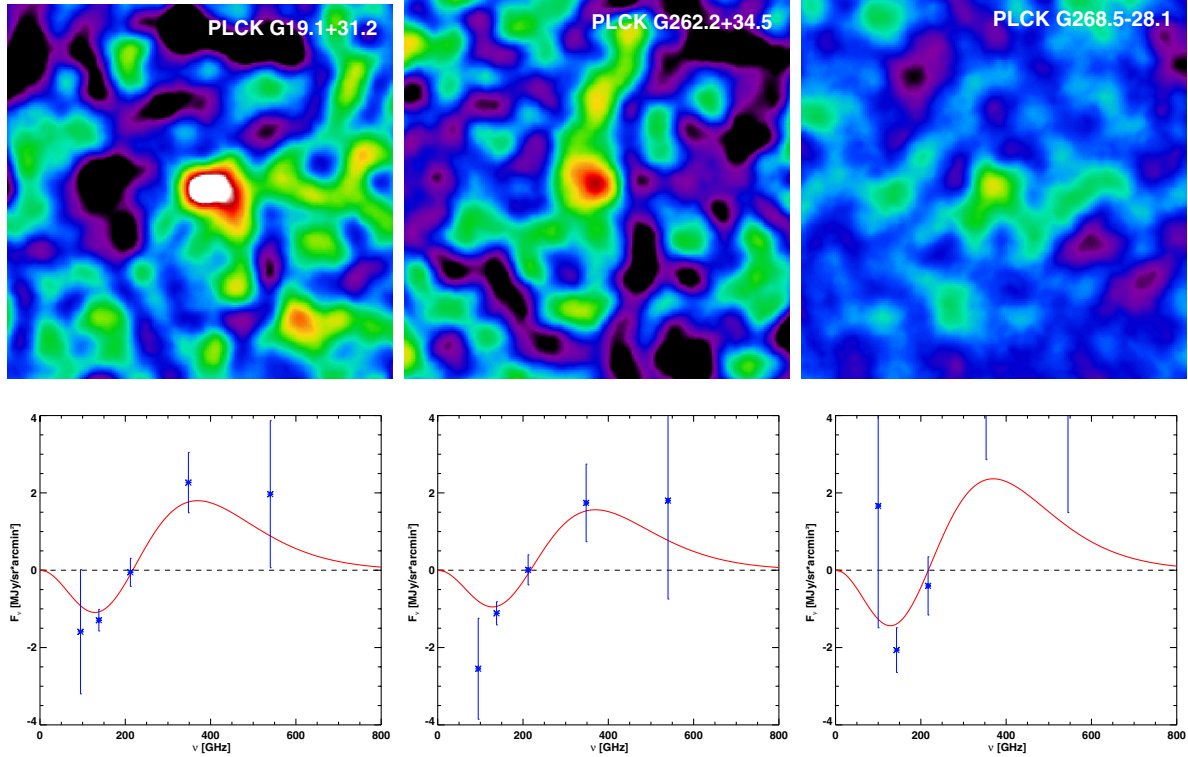
**Fig. 1.** Illustration of the three SZ quality grades as defined in Sect. 2. From left to right the three quality cases are: $Q_{SZ} = A, B, C$. The *top* row shows a $100' \times 100'$ SZ map with a spatial resolution of $10'$, centred on the candidate position, derived using the MILCA reconstruction method (Hurier et al. 2010). The colour table is identical for all clusters, with the Compton $y$ parameter spanning the range $[-3 \times 10^{-6}, 1 \times 10^{-5}]$. The *bottom* row shows the associated SZ spectrum from aperture photometry measurements within $R_{500}$ (see text for details). The red line is the SZ spectrum normalised to the $Y_{500}$ value obtained from MMF blind detection.

"MMF3", developed by Melin et al. (2006). Complementary searches were also performed with an independent implementation of the MMF method and with the PowellSnakes algorithm (PWS; Carvalho et al. 2009, 2011). As described in Planck Collaboration (2011b), candidates then underwent a validation process, including internal SZ quality checks. The first part of this process included an initial quantitative assessment of the blind SZ signal detection, based on the S/N and the number of methods blindly detecting the candidate, $N_{det}$.

The quality of the SZ signal cannot simply be reduced to a single global S/N value. It depends not only on the intrinsic cluster SZ signal, but also on the detailed local properties of the various noise components, i.e., the background (e.g., CIB, CMB) and foreground environments (e.g., galactic dust, synchrotron, free-free emissions). Therefore, beyond the quantitative criteria stated above, we also performed a *qualitative* assessment of the SZ signal based on visual inspection of SZ maps and spectra.

We first examined frequency maps, using both raw maps made directly from the *Planck* all sky data, and maps that had been cleaned of dust emission. We used IRIS-100 $\mu$m (Miville-Deschênes & Lagache 2005) and *Planck* HFI-857 GHz maps as dust templates, and the "dust-cleaned" HFI-217 GHz map as a CMB template. These frequency maps were investigated for strong foreground dust contamination and the presence of submillimetre sources on the high frequency side. Radio source contamination and CMB residuals were searched for at low frequencies. In addition to the frequency maps, reconstructed SZ maps were built using three different reconstruction methods based on Independent Linear Component (ILC) analysis (e.g., Hurier et al. 2010). Finally, SZ spectra were built from the SZ flux estimation at each *Planck* frequency. Spectra were estimated both from the best detection outputs and also directly from aperture photometry on CMB- and dust-cleaned maps.

On the basis of the frequency maps, the reconstructed SZ maps, and the spectra for each cluster, we then defined three SZ quality grades, $Q_{SZ}$:

- $Q_{SZ} = A$, if all the following criteria are fulfilled:
  - clear compact SZ source detected in the SZ map;
  - obvious measurements of the SZ decrement at least at 143 GHz or 100 GHz;
  - low dust contamination (i.e., no increase in the 353 GHz and 545 GHz fluxes in the SZ spectrum or residual dust emission or submillimetre point sources in the frequency map), and a reasonable detection at 353 GHz;
  - no radio source contamination (checked in LFI maps) or CMB confusion (checked in the HFI 217 GHz map).
- $Q_{SZ} = B$, if all the following criteria are fulfilled:
  - visible SZ detection in the SZ map or significant measured SZ signal at 143 GHz. The 100 GHz signal can be more noisy;
  - dust emission well subtracted but for the effect of point source contamination at the cluster location, (i.e., increase of the 353 GHz and possibly the 545 GHz fluxes in the SZ spectrum or residual dust emission or submillimetre point sources in the frequency map) resulting in large uncertainties for dust emission removal;
  - no radio source contamination or CMB confusion.
- $Q_{SZ} = C$, if any of the three following criteria are fulfilled:
  - weak SZ spectral signature (due to large error bars or to inconsistent spectral shape) or visible signal in noisy SZ maps;

**Table 1.** Observation log of the *XMM-Newton* validation follow-up.

| Name | $S/N$ | $N_{det}$ | $Q_{SZ}$ | $RA_{SZ}$ (deg) | $DEC_{SZ}$ (deg) | OBSID | Filter | $t_{exp}$ (ks EPN) | Clean fraction (MOS/EPN) | Confirmed |
|---|---|---|---|---|---|---|---|---|---|---|
| PLCK G060.1+15.6 | 5.3 | 3 | B | 280.279 | 30.930 | 658200901 | MMM | 10.0 | 0.4/0.3 | Y |
| PLCK G200.9−28.2 | 5.2 | 2 | A | 72.564 | −3.002 | 658200801 | TTT | 11.2 | 0.8/0.1* | Y |
| PLCK G235.6+23.3 | 5.2 | 3 | B | 134.032 | −7.719 | 658201301 | TTT | 10.7 | 0.4/0.2 | Y |
| PLCK G113.1−74.4 | 5.1 | 2 | C | 10.161 | −11.706 | 658200601 | TTT | 10.0 | 1.0/0.7 | ... |
| PLCK G262.2+34.5 | 5.1 | 3 | B | 158.596 | −17.342 | 658201001 | MMT | 12.4 | 0.9/0.5 | Y |
| PLCK G268.5−28.1 | 5.1 | 3 | C | 92.855 | −59.611 | 658201101 | TTT | 11.0 | 0.8/0.6* | Y |
| PLCK G266.6−27.3 | 5.0 | 3 | B | 94.027 | −57.791 | 658200101 | TTT | 10.0 | 0.8/0.2* | Y |
| PLCK G019.1+31.2 | 5.0 | 3 | A | 249.143 | 3.153 | 658200301 | TTT | 10.0 | 1.0/0.8 | Y |
| PLCK G193.3−46.1 | 4.9 | 3 | B | 53.960 | −6.985 | 658200401 | TTT | 12.1 | 0.8/0.6 | Y |
| PLCK G234.2−20.5 | 4.7 | 3 | C | 92.747 | −27.544 | 658201201 | TTT | 13.7 | 1.0/0.8 | Y |
| PLCK G210.6+17.1 | 4.6 | 2 | C | 117.214 | 9.688 | 658200501 | TTT | 11.7 | 1.0/0.8 | Y |

**Notes.** Column (1): *Planck* source name. Columns (2), (3): signal-to-noise ratio of the *Planck* cluster candidate detection with the MMF3 algorithm in the v4.1 *Planck*-HFI maps, number of methods blindly detecting the candidate. Column (4): quality grade of the SZ detection (A is best). Columns (5) and (6): right ascension and declination of the *Planck* source (J2000). Columns (7)–(10): *XMM-Newton* observation identification number, filter used, on-source exposure time with the EPN camera and fraction of useful time after cleaning for periods of high background due to soft proton flares (EMOS and EPN camera, respectively). Asterisked objects denote observations affected by a high background level. Column (11): confirmed clusters are flagged.

- strong dust contamination (i.e., high 353 GHz and 545 GHz fluxes in the SZ spectrum or residual dust emission or submillimetre point sources in the frequency map);
- possible contamination by radio sources seen down to the LFI-70 GHz channel.

The three cases are illustrated in Fig. 1. These criteria were checked using the maps and spectra obtained with the different methods described above. Convergence between methods helped us to define the quality grade for each candidate.

We chose candidates to examine our internal SZ quality assessment by exploring lower quality detections than in our previous publications. On the basis of a candidate list detected by at least two algorithms[2], we selected eleven candidates detected at $4.5 < S/N < 5.3$ with the MMF3 algorithm. Here we are sampling a lower S/N regime than in our previous validation run (for which $5.1 < S/N < 10.6$) or in the ESZ sample (for which $S/N > 6$). To investigate the pertinence of our SZ quality grade definitions, we selected typical cluster candidates from the three categories, in the following proportions: two, five, and four, respectively, for $Q_{SZ}$ = A, B and C. The SZ properties of the candidates are given in Table 1. Note that the objects in no way constitute a complete or even statistically representative sample. Hence, we cannot use them to draw any quantitative conclusions regarding, for example, the purity of the parent catalogue.

Two of the three lowest S/N candidates, PLCK G193.3−46.1 and PLCK G210.6+17.1 fall in the Sloan Digital Sky Survey (SDSS) area. They have no counterpart in published SDSS cluster catalogues, but our dedicated algorithm search for galaxy over-densities (Fromenteau et al., in prep.) indicated that they were each possibly associated with a $z > 0.5$ cluster. Inclusion of these two targets allowed us to further test SDSS-based confirmation at high $z$.

## 3. *XMM-Newton* observations

The data analysis and validation procedure is described extensively by Planck Collaboration (2011c). We present only a brief summary in this section.

---

[2] Note that the same candidate list was used to define the ESZ.

### 3.1. Observations and data reduction

The candidates were observed between December 22, 2010 and May 16, 2011. The observation identification number and observation setup are summarised in Table 1. The nominal setup used the THIN filters (unless optical loading needed to be avoided) and extended full frame (EFF) mode for the EPN camera.

Calibrated event lists were produced with v11.0 of the *XMM-Newton* Science Analysis System. Data that were affected by periods of high background due to soft proton flares were omitted from the analysis; clean observing time after flare removal is given Table 1. Three observations are affected by high background levels: PLCK G268.5−28.1, PLCK G200.9−28.2 and PLCK G266.6−27.3. The data treatment for the latter cluster is fully described in Planck Collaboration (2011g). For PLCK G268.5−28.1 and PLCK G200.9−28.2, the particle background after flare cleaning is 2 and 1.7 times higher than nominal for the EPN camera, respectively. The EPN data were thus discarded for the spectroscopic analysis, as this is very sensitive to the background estimate.

The cleaned data were PATTERN-selected and corrected for vignetting as described in Pratt et al. (2007). Bright point sources were excised from the data. The background treatment is as described in Pratt et al. (2010). In the spectroscopic analysis, the cluster component was modeled with an absorbed thermal emission model (MEKAL) with a hydrogen column density fixed at the 21-cm value of Dickey & Lockman (1990).

### 3.2. Candidate confirmation

The confirmation status of each *XMM-Newton* observation is given in Table 1 and the *XMM-Newton* images are shown in Fig. 2. Of eleven targets, ten candidates are bona fide clusters. In each case, the extended nature of the X-ray source, clearly detected within the *Planck* position error box, was confirmed by comparing the surface brightness profile with the *XMM-Newton* point spread function (PSF). The consistency between the SZ and X-ray properties (Sect. 4.3) provided the final confirmation check. The total EPIC count rates in the [0.3−2] keV band of each cluster and the maximum radius of detection are given in Table 2.
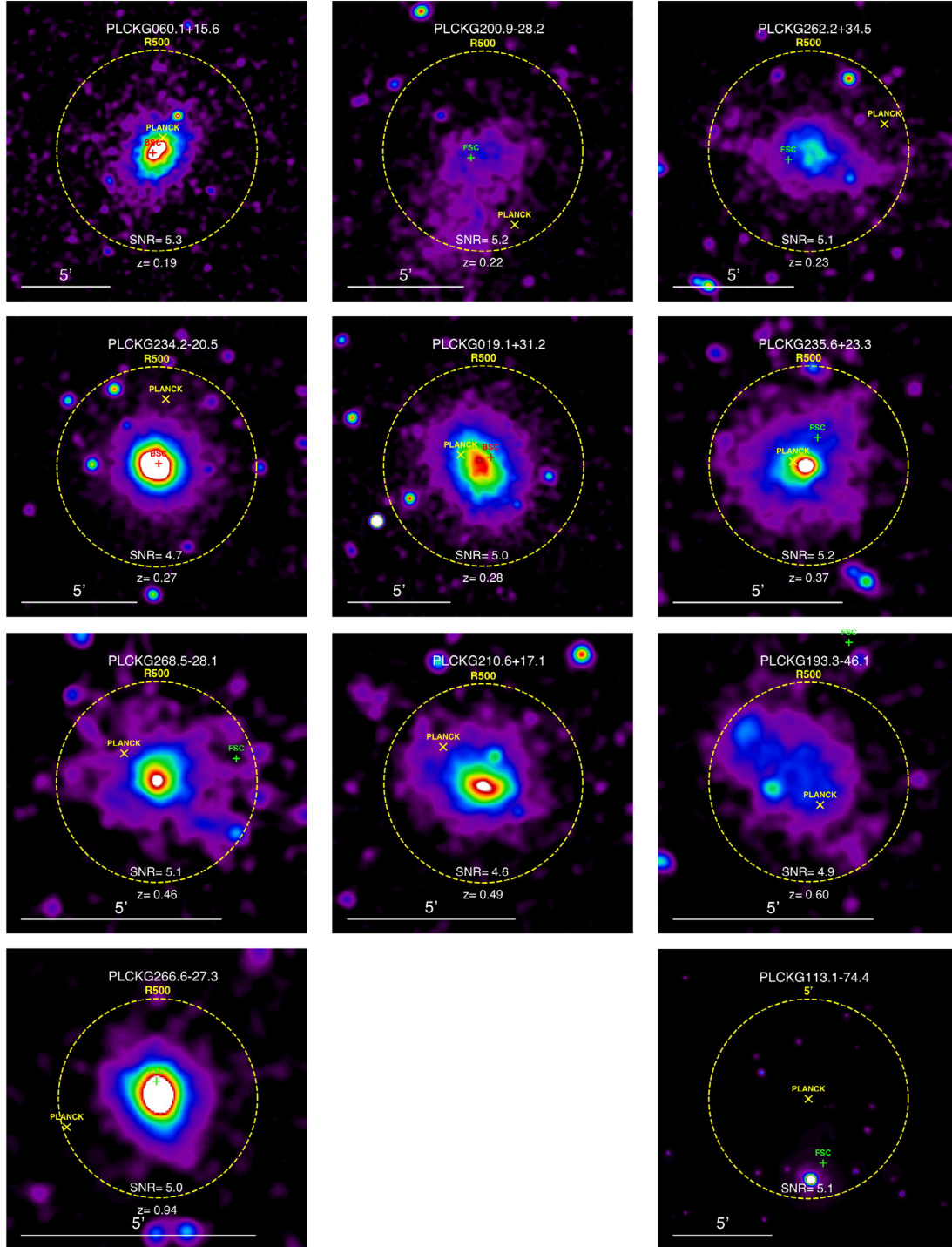
**Fig. 2.** *XMM-Newton* [0.3–2] keV energy band cluster candidate images. North is up and east to the left. The *bottom right-hand panel* shows the image of the false *Planck* candidate. For confirmed clusters, image sizes are $3\theta_{500}$ on a side, where $\theta_{500}$ is estimated from the $M_{500}-Y_{\rm X}$ relation (Eq. (1)). Images are corrected for surface brightness dimming with $z$, divided by the emissivity in the energy band, taking into account galactic absorption and instrument response, and scaled according to the self-similar model. The colour table is the same for all clusters, so that the images would be identical if clusters obeyed strict self-similarity. The majority of the objects show evidence for significant morphological disturbance. A yellow cross indicates the *Planck* position and a red/green plus sign the position of a RASS-BSC/FSC source, respectively.

The offset between the X-ray position and the *Planck* position (Fig. 2) is similar to that observed for known clusters in the ESZ sample (Planck Collaboration 2011b) or for candidates that have previously been confirmed with *XMM-Newton* (Planck Collaboration 2011c). The median offset is 1′6, characteristic of the *Planck* reconstruction uncertainty, which peaks around 2′ (Planck Collaboration 2011b,c) and is driven by the

spatial resolution of the instruments. The largest offset is 3′4 or 0.8 $R_{500}$. This offset is observed for PLCK G200.9−28.2, a highly disturbed cluster with a flat X-ray morphology (Fig. 2), for which a true physical offset between the X-ray and SZ signal may also contribute.

One candidate, PLCK G113.1−74.4, proved to be a false detection (Fig. 2, last panel) as no extended source is detected

**Table 2.** X-ray and SZ properties of the confirmed *Planck* sources.

| Name | $RA_X$ [h:m:s] | $Dec_X$ [d:m:s] | $z_{Fe}$ | $Q_z$ | $R$ [cts s$^{-1}$] | $\theta_{det}$ ['] | $R_{500}$ [Mpc] | $T_X$ [keV] | $M_{gas,500}$ [$10^{14} M_\odot$] | $D_A^{-2} C_{XSZ} Y_X$ [$10^{-4}$ arcmin$^2$] | $Y_{500}$ [$10^{-4}$ arcmin$^2$] | $M_{500}$ [$10^{14} M_\odot$] | $L_{500,[0.1-2.4]\,keV}$ [$10^{44}$ erg s$^{-1}$] |
|---|---|---|---|---|---|---|---|---|---|---|---|---|---|
| PLCK G060.1+15.6 | 18:41:08.5 | +30:55:03.4 | 0.19 | 2 | 1.52 ± 0.03 | 5.4 | 1.07 ± 0.02 | 6.9 ± 0.6 | 0.40 ± 0.02 | 10.9 ± 1.4 | 9.0 ± 2.2 | 4.3 ± 0.3 | 2.65 ± 0.06 |
| PLCK G200.9−28.2 | 04:50:20.9 | −02:56:57.6 | 0.22 | 2 | 0.38 ± 0.03 | 3.1 | 0.91 ± 0.04 | 4.5 ± 0.7 | 0.27 ± 0.02 | 3.8 ± 0.8 | 4.3 ± 3.4 | 2.7 ± 0.3 | 0.99 ± 0.04 |
| PLCK G235.6+23.3 | 08:56:05.9 | −07:43:15.3 | 0.37 | 2 | 0.67 ± 0.02 | 4.9 | 0.95 ± 0.02 | 4.2 ± 0.3 | 0.51 ± 0.01 | 3.2 ± 0.3 | 6.7 ± 1.5 | 3.6 ± 0.2 | 3.50 ± 0.09 |
| PLCK G262.2+34.5 | 10:34:36.2 | −17:21:40.2 | 0.21 | 1† | 0.83 ± 0.02 | 6.0 | 0.91 ± 0.02 | 4.0 ± 0.3 | 0.30 ± 0.01 | 3.8 ± 0.4 | 6.5 ± 2.0 | 2.6 ± 0.1 | 1.42 ± 0.03 |
| PLCK G268.5−28.1 | 06:11:18.9 | −59:37:23.2 | 0.47 | 1* | 0.37 ± 0.01 | 3.3 | 0.83 ± 0.03 | 3.5 ± 0.4 | 0.39 ± 0.02 | 1.6 ± 0.3 | 3.9 ± 0.9 | 2.7 ± 0.3 | 3.39 ± 0.14 |
| PLCK G266.6−27.3 | 06:15:52.1 | −57:46:51.6 | 0.94 | 2 | 0.52 ± 0.02 | 2.3 | 0.98 ± 0.03 | 10.5 ± 1.5 | 1.04 ± 0.02 | 7.0 ± 1.0 | 4.3 ± 0.9 | 7.8 ± 0.6 | 22.7 ± 0.8 |
| PLCK G019.1+31.2 | 16:36:29.8 | +03:08:37.5 | 0.28 | 2 | 1.88 ± 0.02 | 4.1 | 1.24 ± 0.01 | 7.7 ± 0.4 | 0.95 ± 0.03 | 16.0 ± 1.3 | 15.0 ± 2.3 | 7.2 ± 0.3 | 6.24 ± 0.09 |
| PLCK G193.3−46.1 | 03:35:51.4 | −06:58:32.8 | 0.59 | 1‡ | 0.32 ± 0.01 | 2.9 | 0.99 ± 0.03 | 6.0 ± 0.7 | 0.79 ± 0.06 | 4.3 ± 0.8 | 7.1 ± 1.4 | 5.3 ± 0.5 | 5.04 ± 0.17 |
| PLCK G234.2−20.5 | 06:11:01.2 | −27:35:31.7 | 0.27 | 2 | 1.71 ± 0.02 | 4.8 | 1.07 ± 0.01 | 6.1 ± 0.3 | 0.53 ± 0.01 | 7.4 ± 0.4 | 5.2 ± 1.8 | 4.5 ± 0.1 | 4.87 ± 0.05 |
| PLCK G210.6+17.1 | 07:48:46.6 | +09:40:10.6 | 0.48 | 2 | 0.67 ± 0.01 | 4.2 | 1.07 ± 0.02 | 7.0 ± 0.4 | 0.79 ± 0.02 | 6.0 ± 0.5 | 5.5 ± 1.6 | 5.8 ± 0.3 | 6.21 ± 0.11 |

**Notes.** Columns (2), (3): right ascension and declination of the peak of the X-ray emission (J2000). Column (4): redshift from X-ray spectral fitting. Column (5): quality flag for the X-ray redshift measurement (2 is best). Column (6): total EPIC count rates in the [0.3–2] keV band, within the maximum radius of detection given in Col. (7). Columns (8)–(14): $R_{500}$ is the radius corresponding to a density contrast of 500, estimated iteratively from the $M_{500}$–$Y_X$ relation (Eq. (1)), where $Y_X = M_{g,500} T_X$ is the product of the gas mass within $R_{500}$ and the spectroscopic temperature $T_X$, and $M_{500}$ is the total mass within $R_{500}$. $L_{500,[0.1-2.4]\,keV}$ is the luminosity within $R_{500}$ in the [0.1–2.4] keV band. $Y_{500}$ is the spherically integrated Compton parameter measured with *Planck*, centred on the X-ray peak, interior to the $R_{500}$ estimated with the X-ray observations.[†] Other possible $z_{Fe}$: 0.02, 0.82; the best estimate, $z_{Fe} = 0.21$ is consistent with the optical photometric redshift. [‡] Other possible $z_{Fe}$: 0.19, 0.82; the best estimate, $z_{Fe} = 0.59$ is consistent with the optical photometric redshift. [*] Other possible $z_{Fe}$: 0.12, 0.87, 1.20.

within the *Planck* position error. The surface brightness profile of the RASS Faint Source Catalogue source, detected about 5′ South of the *Planck* position, is consistent with that of a point source.

### 3.3. Redshift and physical parameter estimates

To estimate the redshift from the X-ray data, $z_{Fe}$, we extracted a spectrum within a circular region corresponding to the maximum significance of the X-ray detection. Since the centroid of the Fe–K line complex depends on the temperature, the redshift was determined from a thermal model fit to the full spectrum in the [0.3–10] keV band, as described in detail in Planck Collaboration (2011c). The quality of the redshift estimate was characterised by the quality flag $Q_z$ as defined in Planck Collaboration (2011c). The redshift of most clusters is well constrained ($Q_z = 2$). Three clusters, PLCK G193.3−46.1, PLCK-G262.2+34.5 and PLCK G268.5-28.1, have ambiguous $z_{Fe}$ estimates ($Q_z = 1$). They exhibit several $\chi^2$ minima in the $kT$−$z_{Fe}$ plane that do not differ at the 90% confidence level (see Sect. 5.3 for further discussion). For these systems we used the redshift corresponding to the most significant $\chi^2$ minimum, listed in Table 2. For PLCK G193.3−46.1 and PLCK G262.2+34.5, this redshift corresponds to the optical photometric redshift subsequently derived from SDSS data (Sect. 4.2) and our optical follow-up (Sect. 5.1.2), respectively. The uncertainty on the redshift is not propagated through the physical parameter estimation procedure discussed below. The statistical uncertainty on $z_{Fe}$ is small for the $Q_z = 2$ systems. The physical parameters for $Q_z = 1$ systems, especially PLCK G268.5-28.1, are less robust and should be treated with caution.

We then derived the gas density profile of each cluster from the surface brightness profile, using the regularised deprojection and PSF-deconvolution technique developed by Croston et al. (2006). Global cluster parameters were estimated self-consistently within $R_{500}$ via iteration about the $M_{500}$−$Y_X$ relation of Arnaud et al. (2010) assuming standard evolution:

$$E(z)^{2/5} M_{500} = 10^{14.567 \pm 0.010} \left[ \frac{Y_X}{2 \times 10^{14} M_\odot \, \text{keV}} \right]^{0.561 \pm 0.018} M_\odot. \quad (1)$$

The quantity $Y_X$, introduced by Kravtsov et al. (2006), is defined as the product of $M_{g,500}$, the gas mass within $R_{500}$, and $T_X$, where the latter is the spectroscopic temperature measured in the [0.15−0.75]$R_{500}$ aperture. In addition, $L_{500}$, the X-ray luminosity inside $R_{500}$, was calculated as described in Pratt et al. (2009). The errors on $M_{500}$ given in the table correspond to statistical uncertainties only. Additional errors due to scatter around the relation (around 7% from simulations) and uncertainties on the relation itself are not taken into account.

The SZ flux was then re-extracted, calculating $Y_{500}$ with the X-ray position and size $R_{500}$ fixed to the refined values derived from the high-quality *XMM-Newton* observation. The X-ray properties of the clusters and resulting refined $Y_{500}$ values are listed in Table 2. For most cases, the blind values are consistent with the recomputed $Y_{500}$, within the errors. However, as found in our previous studies (Planck Collaboration 2011b,c), there is a trend of SZ flux overestimation with size overestimation. For the present sample, the blind values are overestimated by a median factor of 1.3 for the size and 1.4 for $Y_{500}$.

We have checked for possible AGN contamination using the NVSS (at 1.4 GHz Condon et al. 1998) and SUMSS (at 0.84 GHz Bock et al. 1999) catalogues. A relatively bright radio source (560 mJy) is found in the vicinity of PLCK G193.3−46.1 (at 7.′6 offset). However, LFI data do not show any significant signal so the source must have a steep spectrum. No other radio sources are found in any other candidates. We conclude that no significant contamination of the SZ signal is expected in any of the clusters. However, we cannot exclude the presence of radio faint AGN within each cluster area. Although they could contaminate the X-ray signal if present, the brightest X-ray sources are resolved and excised from the X-ray analysis.

## 4. *XMM-Newton* validation outcome

### 4.1. Planck sensitivity

The present validation run clearly demonstrates the capability of *Planck* to detect clusters of a wide range of masses up to high $z$. All targets in this run fall below the RASS X-ray flux limit. This is illustrated in Fig. 3, where the new clusters are shown
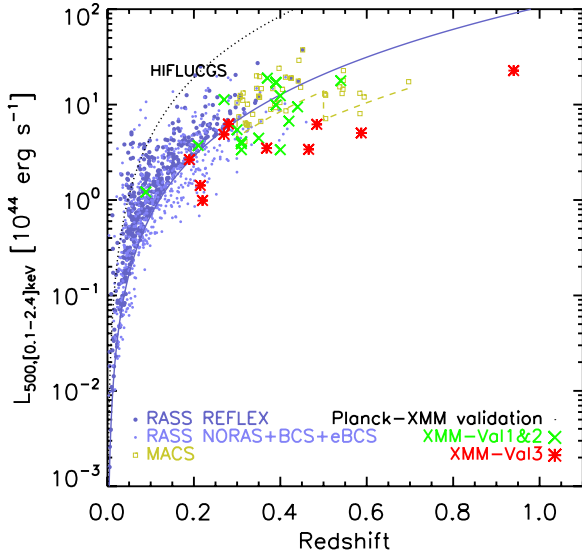
**Fig. 3.** The new SZ-discovered *Planck* objects (red and green symbols) compared to clusters from the ROSAT All-Sky Survey catalogues in the $L_X$–$z$ plane. The X-ray luminosity is calculated in the [0.1–2.4] keV band. Catalogues shown are REFLEX (Böhringer et al. 2004), NORAS (Böhringer et al. 2000), BCS (Ebeling et al. 1998), eBCS (Ebeling et al. 2000) and MACS (Ebeling et al. 2007). The solid line is the REFLEX flux limit, the dotted line is the HIFLUCGS flux limit of $2 \times 10^{-11}$ erg s$^{-1}$ cm$^{-2}$ and the dashed line is from the MACS flux limits.



**Fig. 4.** Regularised scaled density profiles of the new confirmed *Planck* SZ clusters with redshift estimates ($0.2 < z < 0.97$, red lines). They are compared to those of similar mass systems from the representative X-ray samples REXCESS (Böhringer et al. 2007, blue lines), EXCPRES (Arnaud et al., in prep., cyan lines), and the new clusters at lower redshift ($0.09 < z < 0.54$) and higher SZ flux confirmed in previous validation runs (Planck Collaboration 2011c, green lines). The thick lines denote the mean scaled profile for each sub-sample.

in the $L_X$–$z$ plane. They are plotted together with the clusters from large catalogues based on RASS data outside the Galactic Plane and the clusters confirmed in previous *XMM-Newton* validation observations (hereafter *XMM*-Val1&2 ). The new sample covers a wide range of redshift, $0.2 < z < 1$. It includes two clusters at $z > 0.5$ and the first cluster blindly detected by *Planck* at $z \sim 1$ (see Planck Collaboration 2011g, for a detailed discussion of this cluster). The new clusters are less X-ray bright, at a given $z$, than those previously confirmed with *XMM-Newton*. This is not surprising, since we are probing a lower S/N, thus less massive, cluster candidate regime. The new clusters all lie below the RASS survey flux limits, even that of the most sensitive survey (MACS). The mass estimates range from as low as $M_{500} = 2.7 \pm 0.2 \times 10^{14}\ M_\odot$ for the nearby $z = 0.22$ cluster, PLCK G200.9−28.2, to $M_{500} = 7.8 \pm 0.6 \times 10^{14}\ M_\odot$ for PLCK G266.6−27.3 at $z = 0.97$. Interestingly, the two clusters are detected at very similar S/N. This reflects the *Planck* selection function, which depends on the integrated SZ flux, i.e., on the size and redshift of the cluster. *Planck* can detect both (1) low $z$, low mass clusters with large angular extent, and (2) compact high $z$, high mass objects. Consequently, the mass detection threshold of the *Planck* survey increases with redshift (at least in the redshift range probed by the present sample).

### 4.2. Candidate quality assessment

Only one of the eleven candidates, PLCK G113.1−74.4, is false. It is noteworthy that its S/N is the fourth-highest of the sample ($S/N = 5.1$). While this is rather high, its actual SZ detection falls into the lowest quality category, $Q_{SZ} = C$, an indication of the importance of the quality grades defined in Sect. 2, in addition to the S/N. The other three $Q_{SZ} = C$ candidates are confirmed, including PLCK G268.5−28.1, detected at the same S/N as the false candidate, and PLCK G234.2−20.5, detected at $S/N = 4.7$, the second lowest S/N of the sample. Both clusters are detected by all three SZ detection methods, whereas the
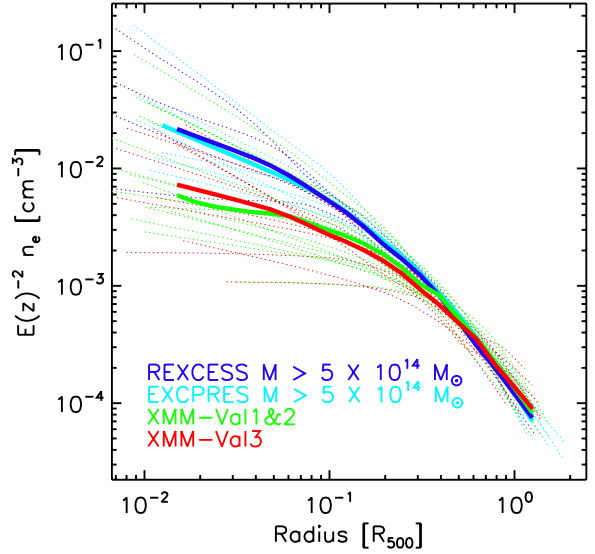
false candidate is only detected with the two MMF methods and not with the PWS algorithm. As expected, the probability that a candidate is a true cluster increases with $N_{\text{det}}$.

As previously noted by Planck Collaboration (2011c), association of a cluster candidate with a RASS source within the *Planck* position uncertainty is not, by itself, sufficient for confirmation. The false candidate, PLCK G113.1−74.4, was associated with a RASS/FSC source that eventually proved to be a point source.

The lowest S/N candidate of all, PLCK G210.6+17.1, is confirmed, whereas it was detected by only two SZ detection methods and lies in the lowest quality category, $Q_{SZ} = C$. However, it is one of the two clusters that was flagged by our SDSS detection algorithm as being possibly associated with an SDSS cluster. The other SDSS cluster candidate, PLCK G193.3−46.1, is also confirmed. The *XMM-Newton* redshift measurements and the photometric redshift[3] of the Brightest Cluster Galaxy (BCG) are fully consistent in the cases where there are matches with SDSS clusters identified by our internal algorithm. For PLCK G210.6+17.1 $z_{\text{phot}} = 0.48 \pm 0.02$ compared to $z_{\text{Fe}} = 0.48 \pm 0.02$. For PLCK G193.3−46.1, $z_{\text{phot}} = 0.65 \pm 0.06$ while $z_{\text{Fe}} = 0.59 \pm 0.02$. This supports the robustness of our SDSS analysis method and indicates that the SDSS can confirm candidates up to $z \sim 0.6$, and estimate their photometric redshifts.

### 4.3. X-ray versus SZ properties of newly detected clusters

The present study samples higher redshifts and lower SZ fluxes than the previous *XMM-Newton* validation observations ($0.2 < z < 0.97$ and $4 \times 10^{-4}$ arcmin$^2 < Y_{500} < 1.5 \times 10^{-3}$ arcmin$^2$, as compared to $0.09 < z < 0.54$ and $6 \times 10^{-4}$ arcmin$^2 < Y_{500} < 3 \times 10^{-3}$ arcmin$^2$ for the previous observations). Our previous findings, detailed in Planck Collaboration (2011c), are

---
[3] The photometric redshift is taken from the PHOTOZ table of the SDSS DR7 galaxy catalogue.

confirmed and extended to higher $z$ and/or lower $Y_{500}$. The new SZ-detected clusters have, on average, lower luminosities, flatter density profiles, and a more disturbed morphology than their X-ray selected counterparts.

The average scaled density profile (Fig. 4) is similar to that of the *XMM*-Val1&2 sample, and remains flatter than that of REXCESS, a representative sample of X-ray selected clusters (Arnaud et al. 2010). The gallery of *XMM-Newton* images (Fig. 2) shows a variety of morphologies with three out of ten clusters exhibiting extremely flat and asymmetric/or X-ray emission. One of those is PLCK G193.3−46.1 at $z = 0.6$, as shown in Fig. 5. Its double peaked X-ray morphology suggests an on-going merger of two sub-clusters along the NE-SW direction, which is supported by the available SDSS data. The galaxy distribution is not centrally peaked and its centroid is 1′.9 South/West of the BCG position. Neither the centre of the galaxy distribution nor the BCG position coincides with any of the X-ray peaks (see Fig. 5).

The new clusters follow the trends in scaling properties established from our previous follow-up (Fig. 6). They are on average less luminous at a given $Y_{500}$, or more massive at a given luminosity, than X-ray selected clusters. Eight out of ten of the new clusters fall on the low luminosity side of the $L_{500}$−$Y_{500}$ relation for X-ray selected clusters (Fig. 6 right panel). As shown in the left hand panel of Fig. 6, the $Y_{500}$−$Y_X$ relation for most clusters remains consistent with the REXCESS prediction:

$$Y_{500} = 0.924 \, D_A^{-2} \, C_{XSZ} \, Y_X, \qquad (2)$$

with $C_{XSZ} = 1.416 \times 10^{-19}$ Mpc$^2$/$M_\odot$ keV. However, the SZ flux levels off around $Y_{500} \sim 4 \times 10^{-4}$ arcmin$^2$. This turnover at low flux is clearly apparent when considering the weighted average $Y_{500}$ values in $Y_X$ bins. It deviates significantly from the prediction in the two lowest $Y_X$ bins, a deviation increasing with decreasing $Y_X$ (grey area in the left panel of Fig. 6). This is reminiscent of the Malmquist bias resulting from a flux cut selection. Due to scatter around the mean relation between the observed flux ($Y_{500}$) and the "true" flux (estimated from $Y_X$), objects below the flux cut are detectable but, in order to be detected, they must be increasingly deviant from the mean relation with decreasing intrinsic flux. The effect is more prominent than that already observed for the *XMM*-Val1&2 sample (Planck Collaboration 2011c), whereas it is negligible for the ESZ-*XMM*-archive sample (Fig. 6). This is likely due to the increasing magnitude of the Malmquist bias as a function of decreasing flux (see also Planck Collaboration 2011e). Note that the scatter in the $Y_{500}$−$Y_X$ relation, and thus the Malmquist bias, is likely dominated by measurements errors. $Y_{500}$ or $Y_X$ are related to the same physical quantity, the thermal energy of the gas. The intrinsic scatter in $Y_{500}$ for a given $Y_X$ is thus expected to be smaller than the <10% intrinsic scatter of either $Y_{500}$ or $Y_X$ values at fixed mass (Kravtsov et al. 2006; Arnaud et al. 2007), and thus smaller than the statistical scatter in the $S/N \lesssim 5$ regime. Outliers are present, though, as discussed below.

The most prominent outliers are the two lowest $D_A^{-2} \, C_{XSZ} \, Y_X$ clusters, PLCK G235.6+23.3 and PLCK G268.5−28.1, which lie at $2.4\sigma$ and $2.8\sigma$, respectively, above the expected relation (Eq. (2)). They could thus be due to statistical fluctuations. However, they correspond to $Y_{500}/Y_X$ ratios 2.1 and 2.5 times higher than expected, respectively. The redshift of PLCK G268.5−28.1 is not well determined and may be under-estimated. We cannot thus exclude that its $Y_X$ value is actually higher (see also Sect. 5.3). On the other hand, PLCK G235.6+23.3 is an unprepossessing cluster at $z = 0.37$
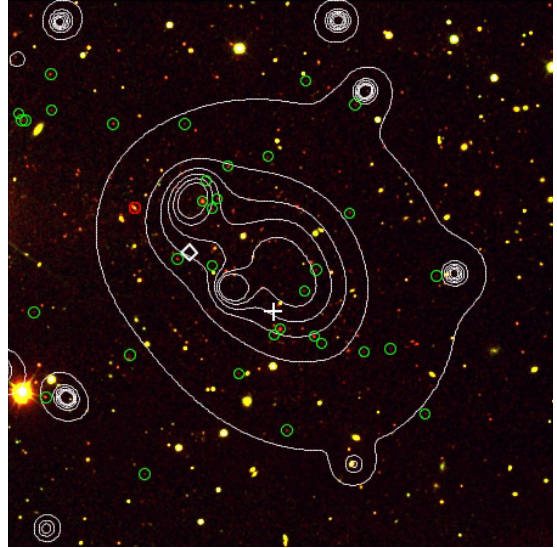


**Fig. 5.** SDSS colour composite image of PLCK G193.3−46.1 at $z = 0.6$ overlaid with isocontours of the wavelet filterered *XMM-Newton* image. The image size is 8′.9 × 8′.9. Green circles: cluster galaxies identified by the search algorithm. Red circle: Brightest Cluster Galaxy. Diamond: centroid of galaxy distribution. Cross: *Planck* SZ position.

with no remarkable X-ray properties, and for which we have very accurate SZ and X-ray measurements. Only one such outlier in terms of $Y_{500}/Y_X$ ratio appears in the ESZ-*XMM*-archival sample of 62 clusters: RXCJ0043.4−2037, a relaxed cluster at $z = 0.29$ (Finoguenov et al. 2005) as can be seen in Fig. 6. A complete follow-up of *Planck* candidates is required to quantify the intrinsic scatter in the $Y_{500}$−$Y_X$ relation and its associated Malmquist bias. Only then can one compare the true dispersion in the $Y_{500}/Y_X$ relation with that established from the ESZ-*XMM*-archival sample.

## 5. Redshift determination

### 5.1. New optical redshift determinations

In this section we present new optical redshift determinations for ten confirmed clusters of the *XMM*-Val1&2 sample and for two of the present sample.

#### 5.1.1. ENO observations

PLCK G171.9−40.7 and PLCK G100.2−30.4 were observed with the 0.82 m IAC80 telescope at the Observatorio del Teide (Tenerife, Spain) as part of a larger campaign for optical follow-up of newly detected *Planck* candidates. Images were taken in four Sloan filters, *griz*, with the CAMELOT camera. This camera is equipped with a 2048 × 2048 pixel CCD (0.304 arcsec per pixel), resulting in a field of view of 10′.4 × 10′.4.

The data reduction included all standard calibrations, i.e., bias and flat field corrections and astrometric calibration. Source detection was undertaken by running SEXTRACTOR (Bertin & Arnouts 1996) on the *i*-band images, and photometry on all bands was obtained in double-image mode. For source detection we used a detection threshold of $3\sigma$ in the filtered maps, which corresponds to a $S/N \sim 6$. All sources classified as stellar objects, based on a stellarity index greater than 0.8 in all bands (given by SExtractor) were excluded from our sample. We applied galactic extinction correction based on the dust maps by Schlegel et al. (1998).
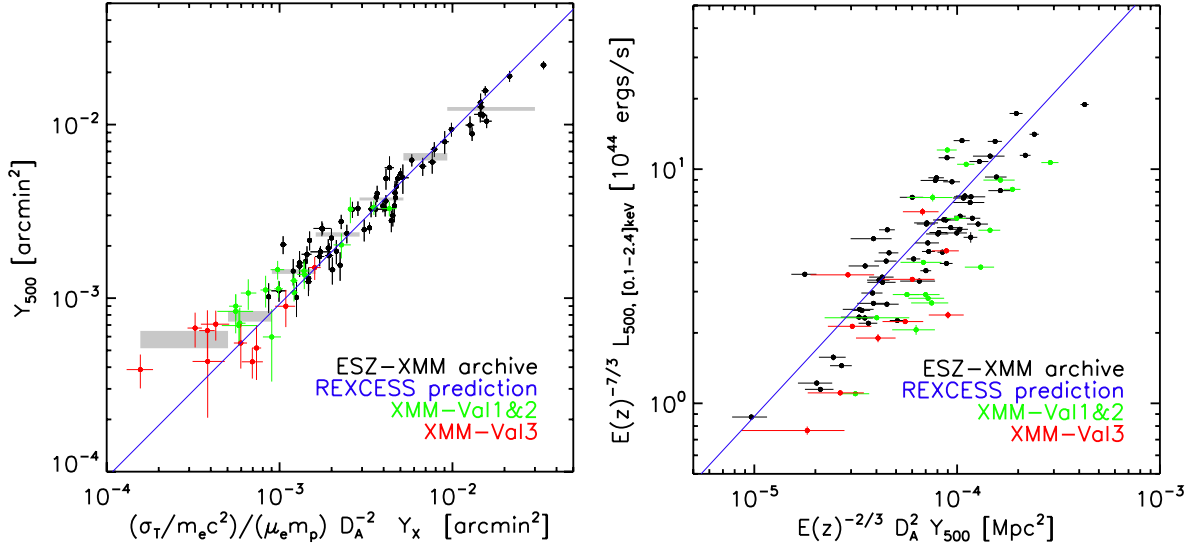
**Fig. 6.** Scaling relations for the ten new confirmed clusters (red symbols). Black points show clusters in the *Planck*-ESZ sample with *XMM-Newton* archival data as presented in Planck Collaboration (2011e); green points represent previously-confirmed *Planck* clusters presented in Planck Collaboration (2011c). The blue lines denote the $Y_{500}$ scaling relations predicted from the REXCESS X-ray observations (Arnaud et al. 2010). *Left*: relation between apparent SZ signal ($Y_{500}$) and the corresponding normalised $Y_X$ parameter. The grey area corresponds to weighted average $Y_{500}$ values in $Y_X$ bins with $\pm 1\sigma$ errors. *Right*: relation between X-ray luminosity and $Y_{500}$. For most data points, uncertainties on the luminosity are smaller than the point size.



**Fig. 7.** Colour composite images (Sloan *gri* filter) of PLCK G171.9-40.7 observed with ENO/ IAC80 telescope. North is up, East is right and the image size is $7'.7 \times 7'.2$. The isocontours of the wavelet filtered *XMM-Newton* image are overlaid.

PLCK G171.9−40.7 was observed in each Sloan *griz* filter in 4000 s exposures. The limiting magnitudes reached are 23.2, 21.1, 20.6 and 20.6 mag for $g, r, i, z$, respectively. The colour composite image in Fig. 7 clearly shows a galaxy overdensity coincident with the X-ray image. The BCG is only slightly offset from the X-ray peak. The final catalogue contains 384 sources, for which we obtained photometric redshifts using the BPZ code (Benítez 2000). The redshift estimate for each individual galaxy is based on all four filters, and is obtained by fitting a set of SED (spectral energy distribution) templates (see details in Benítez 2000). The BPZ code provides the Bayesian posterior probability distribution function (pdf) for the redshift of each object. We have calibrated the code for our set of four filters using a subsample of 5000 galaxies from SDSS DR8 with spectroscopic redshift, $z_{spec,SDSS}$. The standard deviation of the difference between

$z_{spec,SDSS}$ and the photometric redshift, $z_{phot,BPZ}$, obtained applying the BPZ code to this subsample, is $\Delta z = 0.03$. The deviation is similar for the whole sample and for the two different redshift intervals, $0 < z < 0.2$ and $0.2 < z < 0.4$. In a conservative approach, we used this deviation as systematic uncertainty on cluster redshift. The statistical uncertainty is negligible in comparison. For PLCK G171.9-40.7, we use 29 cluster members to infer the photometric redshift, and we obtain $z_{phot} = 0.31 \pm 0.03$.

The data taken for PLCK G100.2−30.4 were already presented in Planck Collaboration (2011c). Images have accumulated integration times of 3000 s in each filter and limiting magnitudes of 22.9, 21.7, 20.1 and 20.2 mag for $g, r, i, z$, respectively. Reduction and catalogue compilation followed the same steps as detailed above for PLCK G171.0−40.7. With respect to the results presented in Planck Collaboration (2011c), the main improvement is that the final images were photometrically re-calibrated using galaxies from SDSS DR8. The initial catalogue contains 452 sources for which photometric redshifts were derived. The object has a photometric redshift of $z_{phot} = 0.34 \pm 0.03$, estimated from the 72 identified cluster members.

### 5.1.2. ESO observations

Optical imaging observations of the *XMM-Newton* confirmed clusters discussed in Planck Collaboration (2011c) were also carried out on the ESO/MPG 2.2 m telescope at La Silla Observatory using the Wide-Field Imager (WFI), which has a field of view of $33' \times 34'$ and pixel size $0''.238$. Each cluster was observed in the $V$, $R$, and $I$-bands in typical seeing conditions of 1.0–1.2″, for total exposure times of at least 0.5 h (consisting of $5 \times 360$ s dithered sub-exposures) per filter. The raw data were calibrated using standard techniques and individual exposures were re-registered and combined using the USNO-B1 catalogue as an astrometric reference. As an illustration, the *VRI* colour composite image of PLCK G262.2+34.5 is shown in Fig. 8.

Galaxies that were simultaneously identified in the combined $V$, $R$, and $I$ images were plotted in a $V - R$ vs. $R - I$
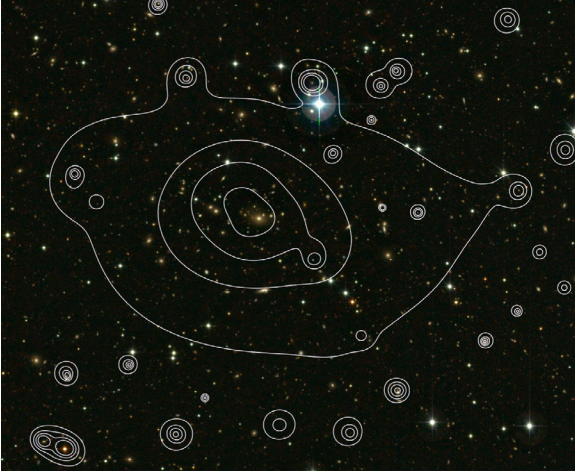
**Fig. 8.** VRI colour composite image of PLCK G262.2+34.5 observed with the ESO/MPG 2.2m telescope, with exposure times of 0.5 h, 1.4 h, and 0.5 h in the *V*, *R*, and *I*-band, respectively. The isocontours of the wavelet filterered *XMM-Newton* image are overlaid. North is up and east to the left, and the image size is $13'.6 \times 11'.1$. Although the X-ray morphology of PLCK G262.2+34.5 is flat rather than centrally peaked, the X-ray centre coincides well with the location of the BCG. The field also contains a large number of X-ray point sources with optical counterparts.

colour–colour diagram. For each cluster, an overdensity of red galaxies, corresponding to the early-type cluster galaxies, was identified in colour–colour space. Galaxies associated with this overdensity in colour–colour space and also spatially coincident (to within ~5′) with the X-ray cluster position were assumed to be early-type cluster members. Predicted $V - R$, $V - I$ and $R - I$ colors of early-type cluster galaxies as a function of redshift were calculated by convolving the "E0" template galaxy spectrum of Coleman et al. (1980) with the combined (filter+CCD) response curves for the *V*, *R* and *I* filters at WFI.

A photometric redshift estimate was then derived by comparing the median $V - R$, $V - I$, and $R - I$ colors of the early-type cluster galaxies to these predictions and averaging the three resulting redshift values. We estimated how typical fluctuations in the photometric zero-point throughout the night translate into uncertainties in the measured $V - I$, $V - R$, $R - I$ colors of galaxies. Given the predicted relation between these colors and the redshift of early-type galaxies, the estimated $1\sigma$ redshift accuracy is $\Delta z = 0.02$. The new photometric redshift estimates for ten clusters observed with WFI are given in Table 3. They were derived from at least 70 photometic redshifts per cluster (mean number of 120).

### 5.2. Comparison between optical and X-ray z estimates

Optical redshifts for twenty *XMM-Newton* confirmed *Planck* clusters are now available. This includes the fourteen measurements presented here or in Planck Collaboration (2011c), values from the literature for the four clusters discovered independently by ACT or SPT (Marriage et al. 2011; Williamson et al. 2011), and two photometric redshifts that we retrieved from SDSS data. The values and references are given in Table 3, together with *XMM-Newton* derived value from the X-ray spectra. For clusters with ambiguous X-ray redshift estimates ($Q_{SZ} < 2$), the values[4] refer to the most significant $\chi^2$ minimum used above to calculate physical properties. The optical and X-ray estimates are compared in Fig. 9. The agreement is excellent, with a weighted
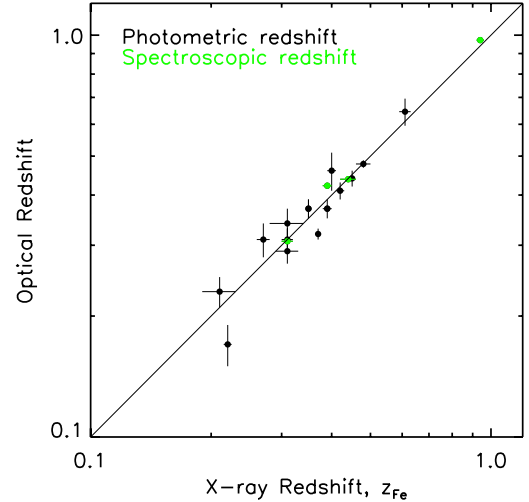
---

[4] The other possible $z_{Fe}$ values are given in the footnote of Table 2.

**Fig. 9.** Comparison between the redshift estimated from optical data and that from *XMM-Newton* spectroscopy.

**Table 3.** Optical redshift data for *XMM-Newton* confirmed clusters.

| Name | $z_{Fe}$ | $z_{opt}$ | Ref. |
|---|---|---|---|
| PLCK G100.2−30.4 | $0.31 \pm 0.03$ | $0.34 \pm 0.03$ | 1 (p) |
| PLCK G171.9−40.7 | $0.27 \pm 0.01$ | $0.31 \pm 0.03$ | 1 (p) |
| PLCK G193.3−46.1 | $0.59 \pm 0.02$ | $0.65 \pm 0.05$ | 2 (p) |
| PLCK G205.0−63.0 | $0.31 \pm 0.01$ | $0.31 \pm 0.02$ | 3 (p) |
| PLCK G210.6+17.1 | $0.48 \pm 0.02$ | $0.478 \pm 0.01$ | 2 (p) |
| PLCK G214.6+37.0 | $0.45 \pm 0.02$ | $0.44 \pm 0.02$ | 3 (p) |
| PLCK G241.2−28.7 | $0.42 \pm 0.01$ | $0.41 \pm 0.02$ | 3 (p) |
| PLCK G262.2+34.5 | $0.21 \pm 0.02$ | $0.23 \pm 0.02$ | 3 (p) |
| PLCK G262.7−40.9 | $0.39 \pm 0.01$ | $0.422$ | 4 (s) |
| PLCK G266.6−27.3 | $0.94 \pm 0.02$ | $0.972$ | 5 (s) |
| PLCK G271.2−31.0 | $0.37 \pm 0.005$ | $0.32 \pm 0.01$ | 5 (p) |
| PLCK G272.9+48.8 | $0.40 \pm 0.01$ | $0.46 \pm 0.05$ | 3 (p) |
| PLCK G277.8−51.7 | $0.44 \pm 0.02$ | $0.438$ | 5 (s) |
| PLCK G285.0−23.7 | $0.39 \pm 0.005$ | $0.37 \pm 0.02$ | 6 (p) |
| PLCK G285.6−17.2 | $0.35 \pm 0.01$ | $0.37 \pm 0.02$ | 3 (p) |
| PLCK G286.3−38.4 | $0.31 \pm 0.01$ | $0.307 \pm 0.003$ | 6 (s) |
| PLCK G286.6−31.3 | $0.22 \pm 0.005$ | $0.17 \pm 0.02$ | 3 (p) |
| PLCK G287.0+32.9 | $0.39 \pm 0.01$ | $0.37 \pm 0.02$ | 3 (p) |
| PLCK G292.5+22.0 | $0.31 \pm 0.02$ | $0.29 \pm 0.02$ | 3 (p) |
| PLCK G334.8−38.0 | $0.35 \pm 0.03$ | $0.37 \pm 0.02$ | 3 (p) |

**Notes.** The references are given in Col. (4), with (s) denoting an optical spectral redshift and (p) a photometric redshift. The redshift from *XMM-Newton* spectral fitting (Planck Collaboration 2011c, or present work) are given in Col. (2) for comparison.

**References.** (1) Present work from ENO/IAC80 observations; (2) SDSS-DR7 data base http://www.sdss.org/dr7/; (3) present work from ESO/MPG2.2 m observations; (4) Sifon et al. (2012) ACT J0438−5419; (5) Williamson et al. (2011); SPT-CLJ0615-5746, SPT-CLJ0549-6204, SPT-CLJ0254-5856, respectively; (6) Planck Collaboration (2011e).

mean ratio of 1.002 and a standard deviation around equality of 0.08. The X-ray and optical spectroscopic redshifts (three clusters) are consistent within $\Delta(z) < 0.02$.

### 5.3. Redshift estimate from a combined X-ray and SZ study

For three clusters in the present sample, PLCK G193.3−46.1, PLCK-G262.2+34.5 and PLCK G268.5-28.1, the X-ray $z$ estimates are ambiguous ($Q_z = 1$) and the spectral fit as a function of $z$ exhibits several $\chi^2$ minima that cannot be distinguished at the 90% confidence level, as illustrated in Fig. 10 (Bottom left
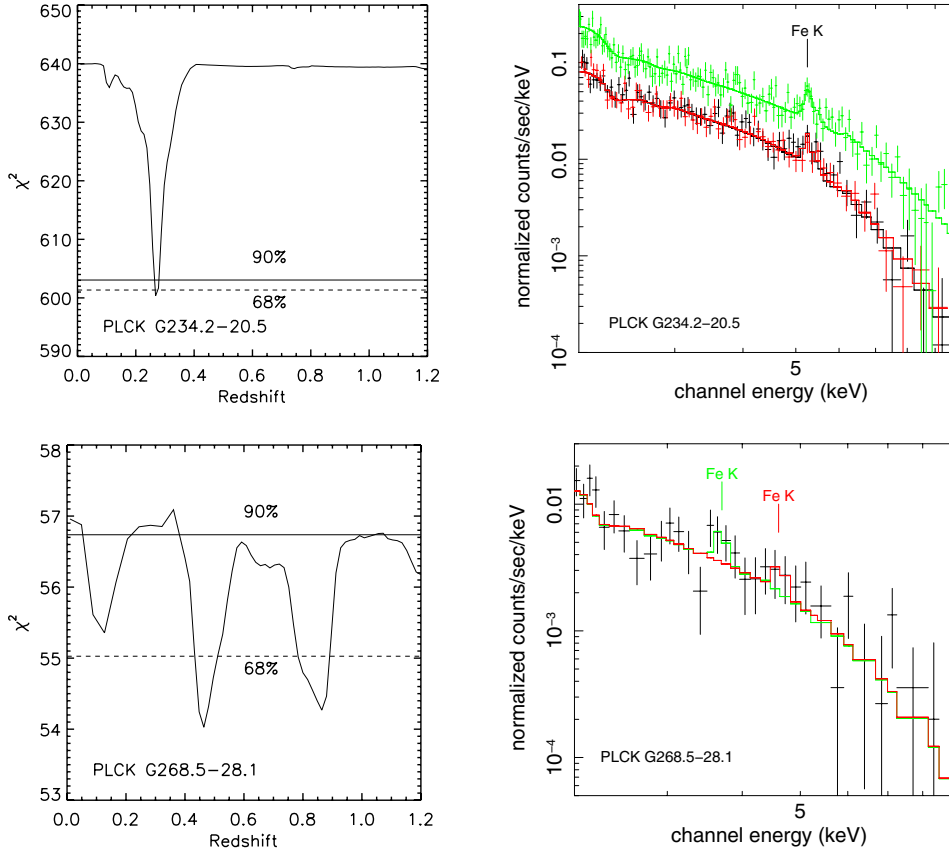
**Fig. 10.** Redshift determination from *XMM-Newton* spectroscopy for the highest quality data (*top row*, PLCK G234.2−20.5) and lowest quality data (*bottom row*, PLCK G268.5-28) in the sample. *Left panels*: variation of $\chi^2$ with $z$ when fitting the EPIC spectra, all other parameters being let free. The dashed and full lines correspond to the 68% and 90% error range, respectively. *Right panels*: EPIC spectra (data points with errors), together with the best-fitting model thermal model (solid lines) with the position of the redshifted Fe K line marked. Only the data points above 2 keV are shown for clarity, but data down to 0.3 keV are used in the spectral fitting. For PLCK G234.2-20.5 (*top right panel*), the Fe-K line complex is clearly detected in the EPIC MOS1&2 (red and black points) and pn (green points) spectra. For PLCK G268.5-28 (*bottom right panel*), only MOS data can be used (see Sect. 3.1) and the spectra are of poor statistical quality. The redshift estimate is ambiguous and the $\chi^2$ distribution (*bottom left panel*) shows several minima. The MOS1&2 spectra, summed for clarity, are compared to the best fitting model for $z = 0.47$ (red line) and $z = 0.86$ (green line), corresponding to the two lowest minima.

panel). This arises when the Fe-K line complex is detected at low significance and statistical fluctuations in the spectra of the same magnitude can mimic the presence of a line (see the bottom right panel of Fig. 10). Low statistical quality data arises because the cluster is intrinsically faint or the X-ray observations are affected by high background conditions. For comparison, the top row of Fig. 10 shows the results for PLCK-G234.2-20.5, for which the data quality are the highest in the sample.

Optical follow-up observations are obviously required to obtain a precise redshift. However, better X-ray redshift estimates are useful for optimising any potential follow-up, e.g., for the use of the most appropriate optical facility or for deciding the pertinence of deeper X-ray follow-up based on known physical properties. In principle, the redshift can be constrained by combining X-ray and SZ data, following a method similar to that used historically to constrain the Hubble constant. The method relies on the different distance dependence of the X-ray and SZ measurements. Here we examined the redshift constraining power of both the $Y_X$–$Y_{500}$ and the $L_X$–$Y_{500}$ relations, using the relations established by Planck Collaboration (2011e) from ESZ clusters with archival *XMM-Newton* data. We consider the three clusters with ambiguous X-ray redshift estimates, including the two clusters, PLCK G193.3−46.1 and PLCK-G262.2+34.5, for which a photometric redshift is available (Table 3). Use of the latter allows us to undertake an internal consistency check.

The X-ray luminosity in the [0.1–2.4] keV energy band scales quasi-linearly with $D_A^2 Y_{500}$. Using the normalisation of the $L_X$–$D_A^2 Y_{500}$ relation and its $z$ dependence, given in Table 2 of Planck Collaboration (2011e), and taking into account the $z$ dependence of the luminosity-distance, one can write:

$$\frac{\left[F_X/10^{-12}\ \text{erg s}^{-1}\ \text{cm}^2\right]}{\left[Y_{500}/10^{-3}\ \text{arcmin}^2\right]} = 4.95\, E(z)^{5/3}\, (1+z)^{-4}\, K(z) \tag{3}$$

where $F_X$ is the X-ray flux at Earth in the same band and $K(z)$ is the K correction. The K correction increases with $z$, with a typical value of $K = 1.24$ at $z = 0.5$ for a $kT = 6$ keV cluster. We can neglect the temperature dependence of the K correction, which is much smaller than the typical dispersion of the $L_X$–$Y_{500}$ relation for the energy band and mass range under consideration.

The theoretical relation is plotted in the left hand panel of Fig. 11. For each cluster, we then estimated the X-ray flux and $Y_{500}$, fixing $z$ to each possible value in turn. The flux estimates depend on physical cluster parameters such as size $\theta_{500}$ and temperature, whose estimate depends in turn on $z$ and requires data of sufficient quality. As can be seen in the figure, in practice the measured flux ratio depends weakly on the assumed $z$. This simply reflects the fact that the fluxes are the quantities most directly related to the raw measurements. If data are of insufficient quality, the ratio can also simply be estimated at a fiducial $z$
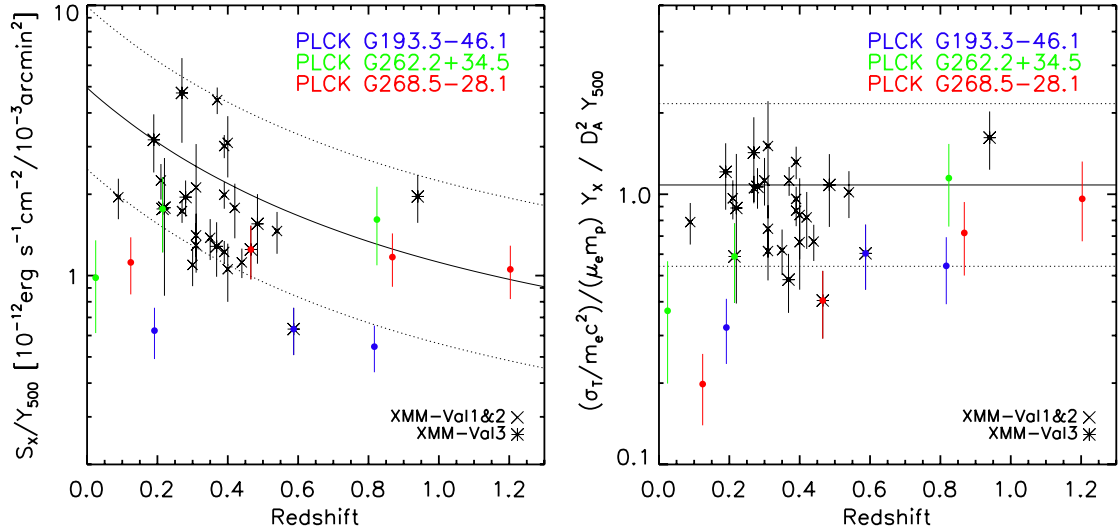
**Fig. 11.** Variation with redshift of the ratio between the X-ray and SZ flux (*left panel*) and between $Y_X$ and $D_A^2 Y_{500}$ (*right panel*). Line: locus established from scaling relations (Planck Collaboration 2011e; Arnaud et al. 2010). The dotted lines correspond to a factor of two above or below the mean relation. Black points: data for new *Planck* candidates confirmed with *XMM-Newton*. Colour points: data for clusters with ambiguous X-ray redshift estimates, one colour per cluster. Each point corresponds to one of the redshift solutions for an individual cluster, as derived from the $\chi^2(z)$ minima (see Fig. 10).

and $kT$. More importantly, since the true ratio depends on $z$, this redshift can be constrained from the measured ratio and Eq. (3). Unfortunately, as can be seen in Fig. 11, the large dispersion around the relation limits the constraints one can achieve with this method. The variation beyond $z \sim 0.2$ is no more than a factor of two, meaning that one cannot distinguish between a factor of two under-luminous outlier at $z = 0.2$ and a "normal" cluster at $z = 1$. The lack of constraining power is exacerbated by the very nature of the clusters in question; those with poor $z$ estimates are generally objects with low intrinsic X-ray fluxes.

We thus also examined the $Y_X–Y_{500}$ relation, which exhibits a lower intrinsic scatter. Planck Collaboration (2011e) showed that the $Y_X–Y_{500}$ relation is consistent with that derived from REXCESS. The $C_{XSZ} Y_X/(D_A^2 Y_{500})$ ratio is fixed from Eq. (2), while its estimate from X-ray and SZ data depends on $z$. This dependence is complex and does not follow a simple analytical law. For each assumed $z$ in turn, the parameters must be derived from X-ray data and SZ data re-processing. The estimated ratio increases with the assumed $z$, as illustrated in the right-hand panel of Fig. 11. Although its dispersion is smaller, the $Y_X–Y_{500}$ relation does not provide better constraints. For newly detected clusters, this method is limited by 1) the large statistical uncertainty of SZ data and 2) the possibility that the cluster is an outlier (this latter being all the more important because of the Malmquist bias). This is perfectly illustrated in the case of PLCK G268.5−28.5. A redshift as low as $z = 0.15$ is very unlikely. However, the cluster could either be at $z = 1.2$ if it perfectly follows the mean relations, or it could be an under-luminous, low $Y_X$ cluster at $z = 0.47$ (the best X-ray estimate). The cases of PLCK G193.3−46.1 and PLCK G262.2+34.5 are very similar: only the lowest $z$ solution can be excluded. On the other hand, the redshifts indicated by optical data, $z_{phot} \sim 0.60$ and $z_{phot} \sim 0.23$, respectively, are indeed allowed by the present analysis. However, higher $z$ solutions yield X/SZ values closest to the theoretical relations. This again illustrates the limitation of the method in the presence of scatter.

In summary, we find that the use of the $Y_X$ vs. $Y_{SZ}$ and X-ray flux $F_X$ vs. $Y_{SZ}$ relations allows us to put lower limits on cluster redshifts.

## 6. Conclusion

We have presented a further eleven *XMM-Newton* X-ray observations of *Planck* cluster candidates, undertaken in the framework of a DDT validation programme. The sample was chosen from blind detections in all-sky maps from the first ten months of the survey and probes lower signal-to-noise and SZ quality criteria than published previously (Planck Collaboration 2011e). Ten of the candidates are confirmed to be *bona fide* clusters, all of which fall below the RASS X-ray flux limit. The objects lie at redshifts $0.22 < z < 0.94$ and have masses (estimated from the $M_{500}–Y_X$ relation) in the range $(2.7 \pm 0.2) \times 10^{14} M_\odot < M_{500} < (7.8 \pm 0.6) \times 10^{14} M_\odot$. We detect a first indication for Malmquist bias in the $Y_{SZ}–Y_X$ relation, with a turnover at $Y_{SZ} \sim 4 \times 10^{-4}$ arcmin$^2$.

This validation run clearly demonstrates the capability of the *Planck* survey to detect clusters of a wide range of masses up to high $z$, although with a mass detection threshold that increases with redshift. We emphasise that the present sample is neither complete not representative, being constructed to sample various SZ quality flags. While it is not a priori biased towards any specific type of cluster, it cannot be used to infer any statistical information on the parent catalogue, such as its underlying purity, or for quantifying the Malmquist bias.

We studied the pertinence of our internal quality grades assigned to the SZ detection, based on visual inspection of the reconstructed 2D SZ maps and SZ spectrum. The single false candidate has a relatively high $S/N \sim 5$, but the lowest SZ quality grade. This confirms that the quality of the *Planck* SZ detection cannot be reduced to a single global S/N and is an indication of the pertinence of our internal quality grade definition. On the other hand, real clusters do have C grade detections. Such a grade is clearly not sufficient to exclude a given candidate. However, A and B grade detections are strong indications for a real cluster.

We presented new optical redshift determinations of candidates previously with *XMM-Newton*, obtained with ENO and ESO telescopes. The X-ray and optical redshifts for a total of 20 clusters are found to be in excellent agreement. We also show that useful lower limits can be put on cluster redshifts

using X-ray data alone via the $Y_X$ vs. $Y_{SZ}$ and X-ray flux $F_X$ vs. $Y_{SZ}$ relations.

In terms of physical properties, the present clusters are similar to the first new *Planck* SZ detections presented in Planck Collaboration (2011e), except at lower $Y_{500}$ and higher mean redshift. The majority show signs of significant morphological disturbance, which is reflected in their flatter density profiles compared to those of X-ray selected systems.They are, on average, under-luminous for their mass as compared to X-ray selected clusters.

In future work, we will explore even lower S/N detections and discuss information from ancillary data, such as that available from SDSS or RASS, as an indicator of candidate validity.

# References

Arnaud, M., Pointecouteau, E., & Pratt, G. W. 2007, A&A, 474, L37
Arnaud, M., Pratt, G. W., Piffaretti, R., et al. 2010, A&A, 517, A92
Benítez, N. 2000, ApJ, 536, 571
Bertin, E., & Arnouts, S. 1996, A&AS, 117, 393
Bock, D., Large, M. I., & Sadler, E. M. 1999, AJ, 117, 1578
Böhringer, H., Voges, W., Huchra, J. P., et al. 2000, ApJS, 129, 435
Böhringer, H., Schuecker, P., Guzzo, L., et al. 2004, A&A, 425, 367
Böhringer, H., Schuecker, P., Pratt, G. W., et al. 2007, A&A, 469, 363
Carlstrom, J. E., Ade, P. A. R., Aird, K. A., et al. 2011, PASP, 123, 568
Carvalho, P., Rocha, G., & Hobson, M. P. 2009, MNRAS, 393, 681
Carvalho, P., Rocha, G., Hobson, M. P., & Lasenby, A. 2011, MNRAS, submitted [arXiv:1112.4886]
Coleman, G. D., Wu, C.-C., & Weedman, D. W. 1980, ApJS, 43, 393
Condon, J. J., Cotton, W. D., Greisen, E. W., et al. 1998, AJ, 115, 1693
Croston, J. H., Arnaud, M., Pointecouteau, E., & Pratt, G. W. 2006, A&A, 459, 1007
da Silva, A. C., Kay, S. T., Liddle, A. R., & Thomas, P. A. 2004, MNRAS, 348, 1401
Dickey, J. M., & Lockman, F. J. 1990, ARA&A, 28, 215
Ebeling, H., Edge, A. C., Bohringer, H., et al. 1998, MNRAS, 301, 881
Ebeling, H., Edge, A. C., Allen, S. W., et al. 2000, MNRAS, 318, 333
Ebeling, H., Barrett, E., Donovan, D., et al. 2007, ApJ, 661, L33
Finoguenov, A., Böhringer, H., & Zhang, Y.-Y. 2005, A&A, 442, 827
Hurier, G., Hildebrandt, S. R., & Macias-Perez, J. F. 2010, A&A, submitted [arXiv:1007.1149]
Kravtsov, A. V., Vikhlinin, A., & Nagai, D. 2006, ApJ, 650, 128
Marriage, T. A., Baptiste Juin, J., Lin, Y., et al. 2011, ApJ, 731, 100
Melin, J., Bartlett, J. G., & Delabrouille, J. 2006, A&A, 459, 341
Mennella, A., Butler, R. C., Curto, A., et al. 2011, A&A, 536, A3
Miville-Deschênes, M., & Lagache, G. 2005, ApJS, 157, 302
Planck Collaboration 2011a, A&A, 536, A1
Planck Collaboration 2011b, A&A, 536, A8
Planck Collaboration 2011c, A&A, 536, A9
Planck Collaboration 2011d, A&A, 536, A10
Planck Collaboration 2011e, A&A, 536, A11
Planck Collaboration 2011f, A&A, 536, A12
Planck Collaboration 2011g, A&A, 536, A26
Planck HFI Core Team 2011, A&A, 536, A4
Pratt, G. W., Böhringer, H., Croston, J. H., et al. 2007, A&A, 461, 71
Pratt, G. W., Croston, J. H., Arnaud, M., & Böhringer, H. 2009, A&A, 498, 361
Pratt, G. W., Arnaud, M., Piffaretti, R., et al. 2010, A&A, 511, A85
Schlegel, D. J., Finkbeiner, D. P., & Davis, M. 1998, ApJ, 500, 525
Sifon, C., Menanteau, F., Hasselfield, M., et al. 2012, ApJ, submitted [arXiv:1201.0991]
Sunyaev, R. A., & Zeldovich, Y. B. 1972, Comm. Astrophys. Space Phys., 4, 173
Williamson, R., Benson, B. A., High, F. W., et al. 2011, ApJ, 738, 139

[1] APC, AstroParticule et Cosmologie, Université Paris Diderot, CNRS/IN2P3, CEA/lrfu, Observatoire de Paris, Sorbonne Paris Cité, 10 rue Alice Domon et Léonie Duquet, 75205 Paris Cedex 13, France
[2] Aalto University Metsähovi Radio Observatory, Metsähovintie 114, 02540 Kylmälä, Finland
[3] Agenzia Spaziale Italiana Science Data Center, c/o ESRIN, via Galileo Galilei, Frascati, Italy
[4] Argelander-Institut für Astronomie, Auf dem Hügel 71, 53121 Bonn, Germany
[5] Astrophysics Group, Cavendish Laboratory, University of Cambridge, J J Thomson Avenue, Cambridge CB3 0HE, UK
[6] Atacama Large Millimeter/submillimeter Array, ALMA Santiago Central Offices, Alonso de Cordova 3107, Vitacura, Casilla 763 0355 Santiago, Chile
[7] CITA, University of Toronto, 60 St. George St., Toronto, ON M5S 3H8, Canada
[8] CNRS, IRAP, 9 Av. Colonel Roche, BP 44346, 31028 Toulouse Cedex 4, France
[9] California Institute of Technology, Pasadena, California, USA
[10] Centre of Mathematics for Applications, University of Oslo, Blindern, Oslo, Norway
[11] Centro de Astrofísica, Universidade do Porto, Rua das Estrelas, 4150-762 Porto, Portugal
[12] Centro de Estudios de Física del Cosmos de Aragón (CEFCA), Plaza San Juan 1, planta 2, 44001 Teruel, Spain
[13] Computational Cosmology Center, Lawrence Berkeley National Laboratory, Berkeley, California, USA
[14] Consejo Superior de Investigaciones Científicas (CSIC), Madrid, Spain
[15] DSM/Irfu/SPP, CEA-Saclay, 91191 Gif-sur-Yvette Cedex, France
[16] DTU Space, National Space Institute, Juliane Mariesvej 30, Copenhagen, Denmark
[17] Departamento de Física Fundamental, Facultad de Ciencias, Universidad de Salamanca, 37008 Salamanca, Spain
[18] Departamento de Física, Universidad de Oviedo, Avda. Calvo Sotelo s/n, Oviedo, Spain
[19] Department of Astronomy and Astrophysics, University of Toronto, 50 Saint George Street, Toronto, Ontario, Canada
[20] Department of Physics & Astronomy, University of British Columbia, 6224 Agricultural Road, Vancouver, British Columbia, Canada
[21] Department of Physics and Astronomy, University of Southern California, Los Angeles, California, USA
[22] Department of Physics and Astronomy, University of Sussex, Brighton BN1 9QH, UK
[23] Department of Physics, Gustaf Hällströmin katu 2a, University of Helsinki, Helsinki, Finland
[24] Department of Physics, Purdue University, 525 Northwestern Avenue, West Lafayette, Indiana, USA
[25] Department of Physics, University of California, Berkeley, California, USA
[26] Department of Physics, University of California, One Shields Avenue, Davis, California, USA
[27] Department of Physics, University of California, Santa Barbara, California, USA

[28] Department of Physics, University of Illinois at Urbana-Champaign, 1110 West Green Street, Urbana, Illinois, USA

[29] Dipartimento di Fisica e Astronomia G. Galilei, Università degli Studi di Padova, via Marzolo 8, 35131 Padova, Italy

[30] Dipartimento di Fisica, Università La Sapienza, P. le A. Moro 2, Roma, Italy

[31] Dipartimento di Fisica, Università degli Studi di Milano, via Celoria 16, Milano, Italy

[32] Dipartimento di Fisica, Università degli Studi di Trieste, via A. Valerio 2, Trieste, Italy

[33] Dipartimento di Fisica, Università di Ferrara, via Saragat 1, 44122 Ferrara, Italy

[34] Dipartimento di Fisica, Università di Roma Tor Vergata, via della Ricerca Scientifica 1, Roma, Italy

[35] Dipartimento di Matematica, Università di Roma Tor Vergata, via della Ricerca Scientifica 1, Roma, Italy

[36] Discovery Center, Niels Bohr Institute, Blegdamsvej 17, Copenhagen, Denmark

[37] Dpto. Astrofísica, Universidad de La Laguna (ULL), 38206 La Laguna, Tenerife, Spain

[38] European Southern Observatory, ESO Vitacura, Alonso de Cordova 3107, Vitacura, Casilla 19001, Santiago, Chile

[39] European Space Agency, ESAC, Camino bajo del Castillo, s/n, Urbanización Villafranca del Castillo, Villanueva de la Cañada, Madrid, Spain

[40] European Space Agency, ESAC, Planck Science Office, Camino bajo del Castillo, s/n, Urbanización Villafranca del Castillo, Villanueva de la Cañada, Madrid, Spain

[41] European Space Agency, ESTEC, Keplerlaan 1, 2201 AZ Noordwijk, The Netherlands

[42] Helsinki Institute of Physics, Gustaf Hällströmin katu 2, University of Helsinki, Helsinki, Finland

[43] INAF – Osservatorio Astronomico di Padova, Vicolo dell'Osservatorio 5, Padova, Italy

[44] INAF – Osservatorio Astronomico di Roma, via di Frascati 33, Monte Porzio Catone, Italy

[45] INAF – Osservatorio Astronomico di Trieste, via G.B. Tiepolo 11, Trieste, Italy

[46] INAF Istituto di Radioastronomia, via P. Gobetti 101, 40129 Bologna, Italy

[47] INAF/IASF Bologna, via Gobetti 101, Bologna, Italy

[48] INAF/IASF Milano, via E. Bassini 15, Milano, Italy

[49] INFN, Sezione di Roma 1, Universit'a di Roma Sapienza, Piazzale Aldo Moro 2, 00185 Roma, Italy

[50] INRIA, Laboratoire de Recherche en Informatique, Université Paris-Sud 11, Bât. 490, 91405 Orsay Cedex, France

[51] IPAG: Institut de Planétologie et d'Astrophysique de Grenoble, Université Joseph Fourier, Grenoble 1 / CNRS-INSU, UMR 5274, 38041 Grenoble, France

[52] Imperial College London, Astrophysics group, Blackett Laboratory, Prince Consort Road, London, SW7 2AZ, UK

[53] Infrared Processing and Analysis Center, California Institute of Technology, Pasadena, CA 91125, USA

[54] Institut d'Astrophysique Spatiale, CNRS (UMR8617) Université Paris-Sud 11, Bât. 121, 91405 Orsay, France

[55] Institut d'Astrophysique de Paris, CNRS (UMR7095), 98 bis Boulevard Arago, 75014 Paris, France

[56] Institut de Ciències de l'Espai, CSIC/IEEC, Facultat de Ciències, Campus UAB, Torre C5 par-2, 08193 Bellaterra, Spain

[57] Institute for Space Sciences, Bucharest-Magurale, Romania

[58] Institute of Astronomy and Astrophysics, Academia Sinica, Taipei, Taiwan

[59] Institute of Astronomy, University of Cambridge, Madingley Road, Cambridge CB3 0HA, UK

[60] Institute of Theoretical Astrophysics, University of Oslo, Blindern, Oslo, Norway

[61] Instituto de Astrofísica de Canarias, C/Vía Láctea s/n, La Laguna, Tenerife, Spain

[62] Instituto de Física de Cantabria (CSIC-Universidad de Cantabria), Avda. de los Castros s/n, Santander, Spain

[63] Istituto di Fisica del Plasma, CNR-ENEA-EURATOM Association, via R. Cozzi 53, Milano, Italy

[64] Jet Propulsion Laboratory, California Institute of Technology, 4800 Oak Grove Drive, Pasadena, California, USA

[65] Jodrell Bank Centre for Astrophysics, Alan Turing Building, School of Physics and Astronomy, The University of Manchester, Oxford Road, Manchester, M13 9PL, UK

[66] Kavli Institute for Cosmology Cambridge, Madingley Road, Cambridge, CB3 0HA, UK

[67] LAL, Université Paris-Sud, CNRS/IN2P3, Orsay, France

[68] LERMA, CNRS, Observatoire de Paris, 61 avenue de l'Observatoire, Paris, France

[69] Laboratoire AIM, IRFU/Service d'Astrophysique – CEA/DSM – CNRS – Université Paris Diderot, Bât. 709, CEA-Saclay, 91191 Gif-sur-Yvette Cedex, France
e-mail: `monique.arnaud@cea.fr`

[70] Laboratoire Traitement et Communication de l'Information, CNRS (UMR 5141) and Télécom ParisTech, 46 rue Barrault, 75634 Paris Cedex 13, France

[71] Laboratoire de Physique Subatomique et de Cosmologie, Université Joseph Fourier Grenoble I, CNRS/IN2P3, Institut National Polytechnique de Grenoble, 53 rue des Martyrs, 38026 Grenoble Cedex, France

[72] Laboratoire de Physique Théorique, Université Paris-Sud 11 & CNRS, Bâtiment 210, 91405 Orsay, France

[73] Lawrence Berkeley National Laboratory, Berkeley, California, USA

[74] Max-Planck-Institut für Astrophysik, Karl-Schwarzschild-Str. 1, 85741 Garching, Germany

[75] Max-Planck-Institut für Extraterrestrische Physik, Giessenbachstraße, 85748 Garching, Germany

[76] Niels Bohr Institute, Blegdamsvej 17, Copenhagen, Denmark

[77] Observational Cosmology, Mail Stop 367-17, California Institute of Technology, Pasadena, CA 91125, USA

[78] Optical Science Laboratory, University College London, Gower Street, London, UK

[79] SISSA, Astrophysics Sector, via Bonomea 265, 34136 Trieste, Italy

[80] SUPA, Institute for Astronomy, University of Edinburgh, Royal Observatory, Blackford Hill, Edinburgh EH9 3HJ, UK

[81] School of Physics and Astronomy, Cardiff University, Queens Buildings, The Parade, Cardiff, CF24 3AA, UK

[82] Space Research Institute (IKI), Russian Academy of Sciences, Profsoyuznaya Str 84/32, 117997 Moscow, Russia

[83] Space Sciences Laboratory, University of California, Berkeley, California, USA

[84] Stanford University, Dept of Physics, Varian Physics Bldg, 382 via Pueblo Mall, Stanford, California, USA

[85] UPMC Univ Paris 06, UMR7095, 98 bis Boulevard Arago, 75014 Paris, France

[86] Universität Heidelberg, Institut für Theoretische Astrophysik, Albert-Überle-Str. 2, 69120 Heidelberg, Germany

[87] Université de Toulouse, UPS-OMP, IRAP, 31028 Toulouse Cedex 4, France

[88] University Observatory, Ludwig Maximilian University of Munich, Scheinerstrasse 1, 81679 Munich, Germany

[89] University of Granada, Departamento de Física Teórica y del Cosmos, Facultad de Ciencias, Granada, Spain

[90] University of Miami, Knight Physics Building, 1320 Campo Sano Dr., Coral Gables, Florida, USA

[91] Warsaw University Observatory, Aleje Ujazdowskie 4, 00-478 Warszawa, Poland